ARTICLE   OPEN

Check for updates

The impact of minor Cr additions in low alloy steel on corrosion behavior in simulated well environment

Kapil K. Gupta [1,2✉], Saber Haratian[1,2], Oleg V. Mishin [1] and Rajan Ambat[1]

Low alloy steel samples with different Cr content (0–3 wt%) have been exposed to simulated well environment. It is revealed that the 3%Cr sample initially has the highest corrosion resistance. However, due to faster formation of a $Fe_xCa_yCO_3$ protective scale in the 0%Cr sample, this sample demonstrates the highest corrosion resistance after 2 days of exposure. While the $Fe_xCa_yCO_3$ scale is also formed in the 1%Cr sample, the scale is weakly adhered and porous, which does not enable good corrosion resistance. Although the scale formation is delayed in a sample with 3 wt%Cr, once it is formed, the presence of Cr-rich phase in this scale provides greater long-term corrosion protection. Localized corrosion attack is observed in the samples with 0% Cr and 1%Cr, whereas the 3%Cr sample shows no sign of localized attack due to initial pre-passivation and the ability to rebuild the protective scale.

INTRODUCTION

Aqueous corrosion caused by the reaction of dry CO_2 with formation water is a critical issue for steel tubulars in oil and gas industry. High pressures of the fluid and elevated temperatures aggravate the corrosion rate and can also result in severe localized corrosion[1,2]. The spontaneous formation and development of protective corrosion products influenced by both material characteristics (microstructure and chemical composition) and environmental parameters (CO_2 content, solution chemistry, pH, temperature, etc.) determine the corrosion resistance of low alloy steels in sweet conditions[3].

Along with supercritical corrosion, similar aqueous corrosion mechanisms are observed in the downhole steel tubulars considered for carbon capture and storage (CCS) applications, when the injected CO_2 comes in contact with water present in the depleted oil and gas reservoir. The captured and injected CO_2 can contain impurities such as H_2O, O_2, SO_x, NO_x, H_2S, etc. that can influence the corrosion behavior. To determine and understand the influence of impurities, it is important to first analyze the corrosion behavior considering pure CO_2 injection.

While several alloys such as Cr13 martensitic stainless steel, Cr22 duplex stainless steel, Cr25 superduplex stainless steel, Cr-Ni austenitic stainless steels and Ni-based alloys[4] can be used as corrosion-resistant pipeline materials, these alloys are too costly for being widely used in low-yield gas fields. Therefore, more cost-effective low alloy steels are commonly used in the oil and gas infrastructure despite their lower corrosion resistance compared to the highly corrosion-resistant metallic materials. The impact of several decisive environmental and metallurgical variables on steel corrosion behavior in CO_2 environments has been the subject of several recent studies[5–11]. It has been shown that the addition of small amounts of alloying elements to low alloy steel is highly beneficial for its corrosion performance[12], with the influence of minor Cr additions (up to 5 wt%) being particularly significant. For example, it has been reported that even a slightly increased Cr content in low alloy steels increases the amount of Cr in the corrosion products, thus making them more protective.

Furthermore, an increase in Cr content can reduce both the uniform corrosion rate and the sensitivity to localized corrosion in CO_2 environments[7,13–19].

The corrosion rate for low-Cr steels (up to 3 wt% Cr) is approximately an order of magnitude lower than that for carbon steels[20–24], while the cost of the low-Cr steels is only 1.5 times higher compared to that of conventional carbon steels. It is known that additions of low amounts of Cr (0.5 to 3wt.%) can effectively improve the corrosion resistance of low alloy steel in CO_2-containing environments at moderately high solution temperatures by forming a stable chromium oxide passive film/protective scale[25–29]. In several previous studies[27], it has been shown that the characteristics of CO_2 corrosion-induced scales developed on the surface of low-Cr steels differ significantly from those in carbon steel. Depending on the type of corrosion product, CO_2 corrosion scales (mainly composed of $FeCO_3$) on the carbon steel are relatively loosely-adhered to the substrate compared to scales formed on low-Cr steel[16,22,30–32]. Takabe et al.[18] studied the CO_2 corrosion behavior of a 5 wt.% Cr steel and showed that after a 24 h immersion test, the Cr concentration in the protective film was roughly 50 wt%, almost ten times higher than that in the steel body. However, the chemical structure of the corrosion scale was not thoroughly investigated. Moreover, it was recently reported[33] that a 3 wt.% Cr steel displayed pre-passivity at 80 °C during polarization measurements. The pre-passivity observed in this steel directly leads to a reduced rate of material dissolution as compared to that in carbon steel[34].

Based on the positive effect of minor Cr additions on corrosion resistance of carbon steels, an attempt has recently been made to utilize low-Cr alloy steel (0.5–3 wt% Cr) in CO_2 conditions without employing corrosion inhibitors[19,35]. It should be noted that the tests were conducted in only an extremely narrow range of environmental parameters (CO_2-saturated NaCl solution without the addition of other metallic ions)[12]. However, the produced water chemistry in oil wells shows the presence of alkaline earth metallic ions such as Ca^{2+}, Ba^{2+}, etc. in the brine solution. Moreover, it has been hypothesized that an amorphous chromium

[1]Section of Materials and Surface Engineering, Department of Civil and Mechanical Engineering, Technical University of Denmark, 2800 Kgs Lyngby, Denmark. [2]These authors contributed equally: Kapil K. Gupta, Saber Haratian. ✉email: kkgup@dtu.dk

compound together with the siderite forms a protective layer[16,26], however, the mechanism of how Cr improves the CO_2 corrosion resistance is still not fully understood. Therefore, it is necessary to assess the impact of Cr additions on the corrosion behavior of the low alloy steel in conditions simulating the environments at the bottom of the well. To achieve this goal, the CO_2 corrosion behavior of three samples of the API L80 steel with Cr content in the range 0–3 wt% are studied in this work using electrochemical techniques such as potentiodynamic polarization, linear polarization resistance and electrochemical impedance spectroscopy. In addition, a variety of characterization techniques such as X-ray photoelectron spectroscopy, scanning electron microscopy, X-ray diffraction and X-ray tomography are used here to analyze the chemical and physical properties of the scales formed on the steel surface.

RESULTS

Microstructure of the as-received samples

X-ray diffractograms for the as-received samples are shown in Fig. 1. It is seen that all the samples contain ferrite and cementite Fe_3C, which is characteristic of tempered martensite (TM). No other phase is detected by X-ray diffraction (XRD). As expected, TM structures with fine boundary spacings and dispersed cementite particles are observed in scanning electron microscopy (SEM) images (see Fig. 2a, c, e). Quantitative electron backscatter diffraction (EBSD) analysis indicates that the microstructure is much finer in sample 1Cr than in the other two samples (see Fig. 2b, d, f). The average spacing between high angle ($>15°$) boundaries, i.e. grain size, is 1.5 μm and 1.3 μm in sample 0Cr and sample 3Cr, respectively, but only 0.6 μm in sample 1Cr. It is believed that the differences in the microstructure of the samples are caused by different heat treatments applied by material suppliers.

X-ray photoelectron spectroscopy (XPS) data

Figure 3 shows high-resolution X-ray photoelectron spectra and an XPS depth profile measured for the mechanically polished 3Cr sample before exposure to the electrolyte. The peaks in Fig. 3a obtained from the deconvolution of the Fe 2p spectra[36–38] correspond to Fe, oxides, hydroxides and a satellite peak of iron. Sim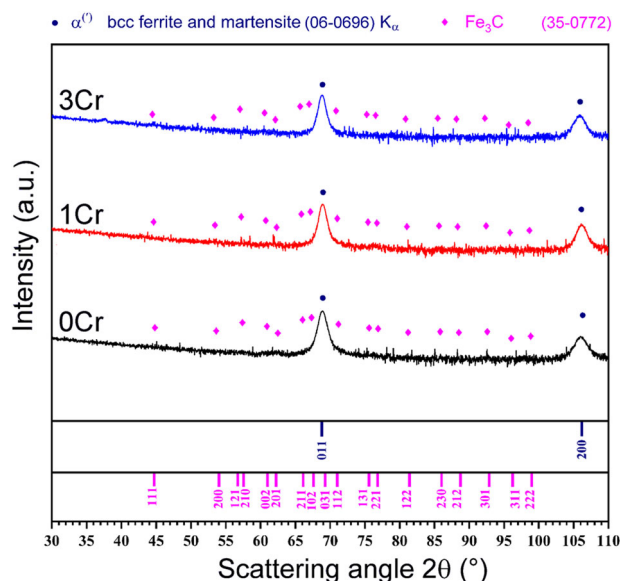ilarly, the deconvolution of Cr 2p spectra (Fig. 3b) reveals peaks corresponding to Cr hydroxides and a satellite peak of Cr[39]. Based on the data presented in Fig. 3c, d, it is found that the polished surface is covered by oxides/hydroxides of Fe and Cr, while below the surface (<10 nm depth), peaks corresponding to elemental Fe and Cr are observed. This suggests the presence of a very thin film of pre-passivating FeO(OH) and Cr(OH)$_3$ layers on the surface of each sample.

Linear polarization resistance (LPR) measurements

The results from the LPR measurements of the samples tested in the simulated produced water are presented in Fig. 4a. Here R_p is the polarization resistance and the error bars represent the maximum and minimum R_p values observed in repeated experiments. The results show that the initial corrosion resistance and the rate of corrosion strongly depend on the Cr content. The LPR results can be divided into two main stages: I - decreasing trend (material dissolution); and II - increasing trend (scaling). The R_p vs time curve shows initially higher corrosion resistance for sample 3Cr; however, after about 24 h the polarization resistance for sample 0Cr increases drastically and becomes much larger than that for sample 3Cr. The significant increase in R_p for sample 3Cr is only observed after 140 h of exposure as opposed to that observed after ~24 h for sample 0Cr. Sample 1Cr shows a sharp drop in R_p (similar to that in sample 0Cr, see the inset in Fig. 4a), followed by a very slow increase in the polarization resistance after ~48 h.

The samples with either the minimum or the maximum concentrations of Cr, i.e., sample 0Cr and sample 3Cr, were exposed to the electrolyte for 28 days to allow scale formation and
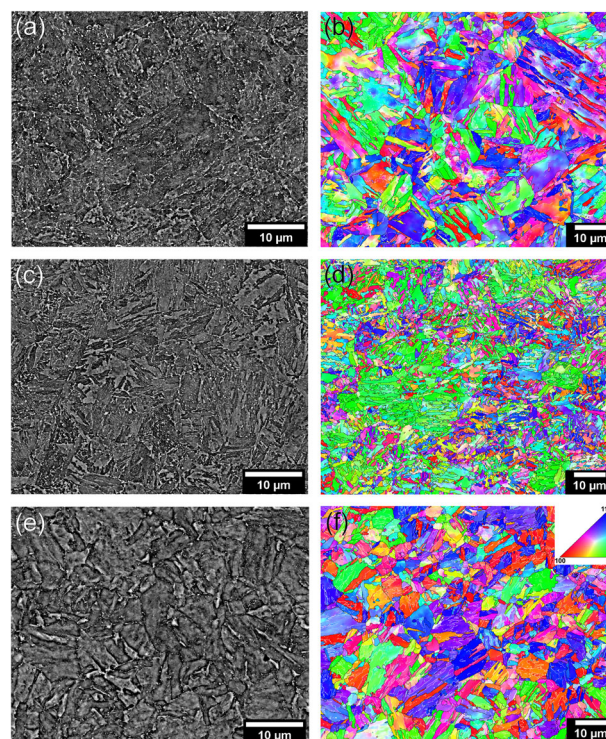

Fig. 2 **Microstructural features of the samples before exposure to electrolyte.** Backscattered electron images (**a**, **c**, **e**) and orientation maps (**b**, **d**, **e**) showing the microstructure of the as-received samples: (**a**, **b**) sample 0Cr; (**c**, **d**) sample 1Cr; (**e**, **f**) sample 3Cr. Note that the SEM images were taken from the etched surface, while EBSD data were collected after eletropolishing of the surface. The inverse pole figure (IPF//Y) color code for orientations of cubic crystal structures is shown in the inset in (**f**). White and black lines in (**b**, **d**, **f**) show boundaries with misorientation angles of 2–15° and high angle ($>15°$) boundaries, respectively.

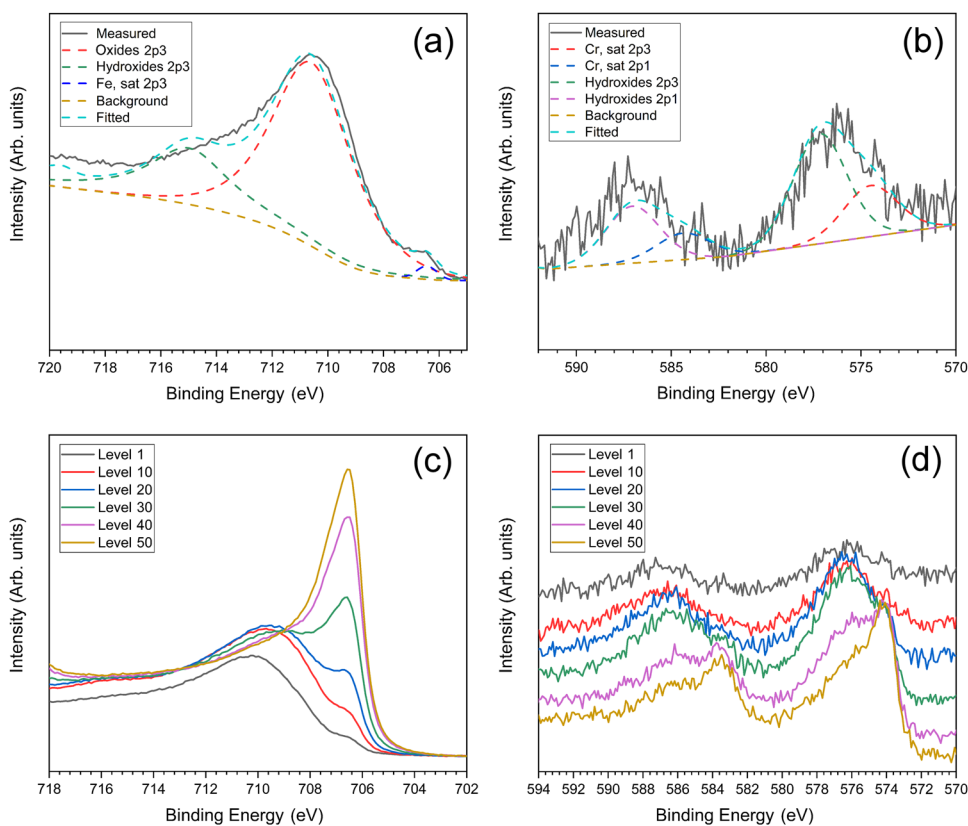Fig. 1 X-ray diffractograms for the different samples prior to corrosion tests.

Fig. 3 Surface analysis of the 3Cr sample using XPS to understand the chemistry and extension of film present on the sample before exposure. High-resolution X-ray photoelectron spectra: (**a**, **c**) Fe 2p and (**b**, **d**) Cr 2p spectra obtained from the surface of the polished sample 3Cr; (**c**, **d**) XPS depth profile analysis after different levels of ion beam etching. The number N for each level corresponds to different time (N×5 s) of ion beam etching (see subsection 5.3.3).

to observe its influence on the corrosion resistance. The results from the LPR measurements for samples 0Cr and 3Cr exposed for 28 days are presented in Fig. 4b. It is seen that for sample 0Cr, a sharp increase in R_p within 6–7 days of exposure is followed by a smaller increase. For sample 3Cr, R_p is initially lower than in sample 0Cr (except the first 2 days) and is followed by a sharp increase, such that after almost 20 days of exposure this sample becomes more corrosion resistant than sample 0Cr. However, the scale adherence for sample 3Cr is very poor and the scale spalls after drying.

Electrical impedance spectroscopy (EIS) analysis

Figure 5 shows impedance spectra corresponding to the corrosion behavior presented in the form of Nyquist plots after every 24 h of exposure. The Nyquist diagrams are obtained to measure the interfacial electrical resistance of the specimens in CO_2-saturated electrolyte, thereby determining the CO_2 corrosion behavior and scaling.

In general, the Nyquist plots show two loops with different amplitudes. At high to medium frequencies (HF-MF), a large semicircle representing material resistance to charge transfer is observed in Fig. 5. The second loop at low frequencies (LF), which is characteristic of either intermediate reactions or scaling, is different for the different samples and changing over time for each sample. The compressed semi-circular shape at HF-MF in the Nyquist plots indicates non-ideal double layer capacitive behavior due to surface roughness. The diameters of the semicircles, which are equivalent to the resistance to corrosion reactions, are also different for the different samples.

For sample 0Cr, the Nyquist plot obtained after 1 h of exposure shows a large semi-circular loop at HF-MF

corresponding to charge transfer resistance, followed by an inductive pseudo-capacitive loop at LF. At longer exposures, instead of an inductive pseudo-capacitive loop, a non-ideal capacitive loop corresponding to the protective scale formation is observed. The diameter of both the semi-circular loop seems to be increasing over time, suggesting an increase in corrosion resistance. Similar behavior is observed for sample 1Cr; however, the non-ideal capacitive loop at LF is observed only after 48 h. Also, the diameters of both the HF and LF loops for sample 1Cr are smaller than those for sample 0Cr. In contrast to the two other samples, sample 3Cr shows an inductive pseudo-capacitive loop at LF along with a capacitive loop at HF-MF over the entire exposure period.

The EIS spectra for corroding steel substrates can be further analyzed using numerical fitting combined with the equivalent electrical circuit to quantify the corrosion behavior. The Nyquist curves with the inductive pseudo-capacitive loop at LF were fitted using the equivalent circuit shown in Fig. 6a, while the Nyquist curves with the capacitive loop at LF (corresponding to protective scale development) were fitted using the equivalent circuit shown in Fig. 6b. The equivalent circuit in Fig. 6a is a simple Randle's system consisting of a double-time constant representing a homogeneous interface, solution resistance R_s, double layer capacitance Q_{dl} and a charge transfer resistance R_{ct} in parallel with inductor resistance R_L as well as the inductance L corresponding to the electrical connections/intermediate reactions. An RC circuit (R_{film} in parallel to Q_{film}) in Fig. 6b due to scale development is attached parallel to the equivalent circuit in Fig. 6a. The Nyquist results fit well with the equivalent circuits using the Randomize+Simplex function. The fitting parameter $\chi^2/|z|$ in Eq. 1
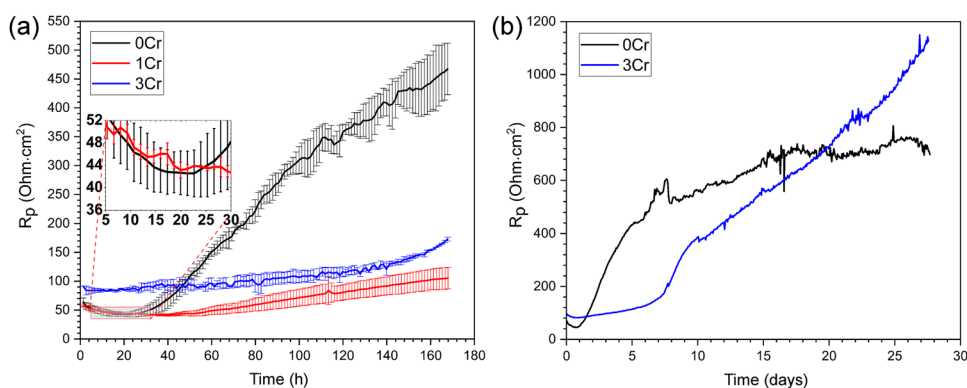
Fig. 4 Insitu corrosion behavior of the samples as determined using LPR technique. Linear polarization resistance over time for the samples exposed to the electrolyte for (**a**) 7 days and (**b**) 28 days.

is less than 0.1, thus indicating a good fit.

$$\frac{\chi^2}{|z|} = \sum_{i=1}^{n} \frac{|Z_{meas}(i) - Z_{Simul}(f_i, param)|^2}{|Z_{meas}(i)|} \qquad (1)$$

where $Z_{meas}(i)$ is the measured impedance at the f_i frequency, $Z_{Simul}(f_i, param)$ is the function of the chosen model, and "param" corresponds to the model parameters (e.g., R1, R2, C1, Q1, …).

Considering the data in Fig. 6c, it is evident that the R_{ct} vs time curve is similar to the LPR curves presented in Fig. 4. Samples 0Cr and 1Cr initially show a sharp drop in material resistance to corrosion reactions R_{ct}, followed by a steady increase. However, sample 3Cr shows a slow increase in R_{ct} over a long time period. The Q_{dl} vs time curve (indicating the development of anodic surface over time) shows an initial sharp increase in Q_{dl} values for samples 0Cr and 1Cr (Fig. 6d), which suggests the generation of a rough surface due to material dissolution. Following the sharp increase, sample 0Cr demonstrates a decrease in Q_{dl}, probably due to blockage of anodic sites by corrosion products, while sample 1Cr shows a constant increase in Q_{dl} due to continuous material dissolution. On the other hand, a low and almost constant Q_{dl} is observed for sample 3Cr (see Fig. 6d).

As mentioned previously, the Nyquist plots for sample 3Cr do not show a capacitive loop at LF, and scale-related individual components are not observed for this sample. The R_{film} vs time curves for samples 0Cr and 1Cr show an increasing trend over time (Fig. 6e), which suggests lower film resistance and increasing film compactness. The rate of increase in R_{film} for sample 0Cr is much higher than for sample 1Cr, confirming greater scale protectiveness for the 0Cr material. The Q_{film} value is characteristic of scale thickness and shows a decreasing trend over time, suggesting thickening of the scale (Fig. 6f). Sample 0Cr demonstrates much lower Q_{film} values compared to sample 1Cr, which indicates a thicker scale for sample 0Cr.

X-ray microscopy (XRM)

Figure 7 shows the results of the XRM examination of the samples exposed to the electrolyte for 7 days. In this figure, a 3D representation of the investigated volumes is shown with differential contrast based on material density. Here the high-density steel appears bright, while the surface consisting of less dense corrosion products is darker.

As is evident from Fig. 7a, the top surface of sample 0Cr is affected by directional corrosion, with scales present in crevices of the corroded area. The 3D reconstruction of the sample without the scale is shown in Fig. 7b, where the scale layer was removed digitally based on its lower density compared to steel. This figure demonstrates surface grooves extended along the longitudinal axis of the sample, which provides clear evidence that corrosion of this sample is highly selective. In addition to the grooves, globular-

shaped pits/craters (localized corrosion) are also seen on the corroded surface. Figure 7c depicts a computer-generated longitudinal section of the sample, which shows the presence of corrosion products over the ragged scale/substrate interface.

Compared to sample 0Cr, the corrosion scale on sample 1Cr is more poorly adhered to the surface and contains long cracks propagating throughout the entire thickness of the scale (see Fig. 7d). Considering the scale-free reconstruction in Fig. 7e, it is seen that the steel surface of sample 1Cr is more uniformly corroded compared to that of sample 0Cr, with some signs of localized attacks in the form of globular pits/craters. Inspection of the longitudinal section of sample 1Cr (Fig. 7f) reveals that the corrosion scale is thick and porous. Furthermore, the scale shows a variation in contrast through the thickness, suggesting the presence of corrosion products with different densities. Close to the steel surface, the corrosion layer is highly porous and is followed by a slightly denser layer containing a thicker scale. The outer shell is formed by another (thinner) layer.

The 3D reconstruction of the studied region of sample 3Cr (Fig. 7g) reveals a cracked porous scale built on the top of the steel surface. The scale porosity extends to the thin outer layer (see Fig. 7i). Figure 7h shows that the surface of this sample is corroded uniformly over the entire analyzed region with no sign of localized corrosion of the steel.

Phase analysis and SEM characterization of the corroded surface

X-ray diffractograms and SEM images of the samples after exposure to the electrolyte are presented in Figs. 8, 9. The X-ray diffractograms (see Fig. 8) reveal the presence of different crystalline corrosion products on the sample surface. The corrosion scale majorly comprises of siderite $FeCO_3$, calcite $CaCO_3$ and cementite Fe_3C for samples 0Cr and 1Cr. Both the $FeCO_3$ and the $CaCO_3$ peaks for sample 0Cr are slightly shifted from their respective reference lines, suggesting the formation of mixed carbonates. For sample 1Cr, a shoulder is seen on the shifted (104) $CaCO_3$ peak. The position of this shoulder matches the position of the reference line for $CaCO_3$. Compared to sample 1Cr, the amount of Fe_3C residue on the surface of the corroded sample 0Cr is higher considering the acquired diffracted intensity (and/or peak area) for this phase. Sample 3Cr reveals less corrosion products present in the scale than samples 0Cr and 1Cr. Small siderite and calcite peaks are observed for the corrosion scale on sample 3Cr, while cementite is not detected in the scale. In addition, a small NaCl peak is observed for all the samples because NaCl present in the brine solution could not be fully removed from the scale. The (104) $CaCO_3$ peak is not shifted in sample 3Cr.

Figure 9 represents the top surface morphology of the sample surfaces after CO_2 corrosion. The surface of the corroded 0Cr
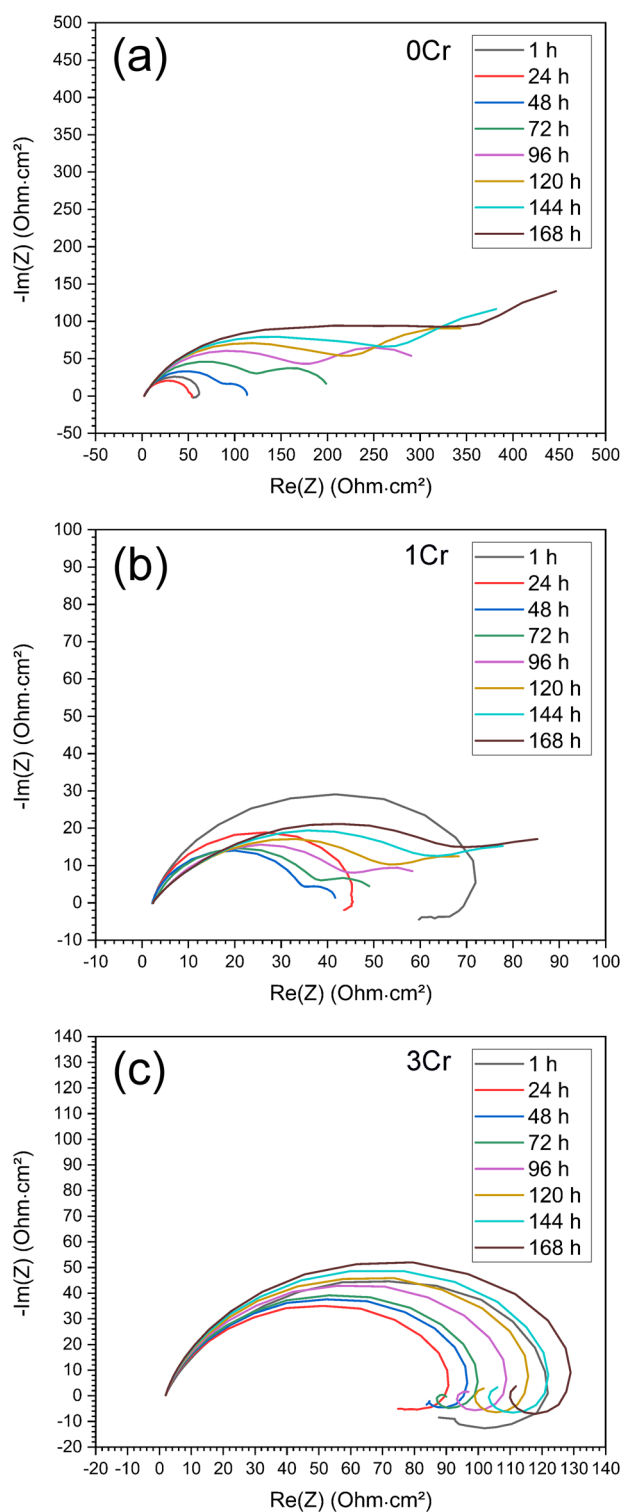
Fig. 5 EIS spectra of the samples during exposure revealing changes in corroding system over time. Nyquist plots recorded during exposure of the samples to the electrolyte: (**a**) sample 0Cr; (**b**) sample 1Cr and (**c**) sample 3Cr.

sample (Fig. 9a) shows evidence of directional selective corrosion and the scales embedded within crevices of the corroded regions. The corrosion product is comprised of small cuboidal particles, which can be $Fe_x(Ca)_yCO_3$ or NaCl crystals as suggested by the energy dispersive spectroscopy (EDS) analysis (see Supplementary

Fig. 1). These crystals with average sizes of ~5 µm uniformly cover the whole sample surface. The SEM image in Fig. 9b shows a thick and dense $Fe_x(Ca)_yCO_3$ layer and small $Fe_x(Ca)_yCO_3$ particles on top of this layer, which is consistent with the XRM images. Below this thick and dense layer, a porous layer comprising different phases is observed. Based on the EDS mapping and XRD data, it is considered that the layer contains a combination of $CaCO_3$ and akagenite $Fe_8O_8(OH)_8Cl_{1.35}$. The interface between the scale and the steel surface is irregular, as is also shown in the XRM images.

For sample 1Cr, clusters of irregular-shaped particles rich in Ca, C and O (see Supplementary Fig. 2) are seen on the top surface of the corroded layer (Fig. 9c). Some evidence of directional corrosion is also observed in this sample though it is not as pronounced as in sample 0Cr. SEM images from the longitudinal section of sample 1Cr (Fig. 9d) present a thick porous layer with varying contrast through the thickness, which is due to compositional variation as confirmed by the EDS analysis (see Supplementary Fig. 3). The corrosion products can be separated into three different zones similar to the results obtained by XRM. The layer closest to the steel surface is rich in Ca, C and O, highly porous and weakly adhered to the substrate. Based on the XRD and EDS results, this porous layer is considered to be $CaCO_3$. A more compact $CaCO_3$ layer is observed on top of the first layer. In the topmost layer, two different types of clustered corrosion products are present. One of them is rich in Fe, O and Cl, while the other one is rich in Fe, Ca, C and O. Based on the EDS maps and XRD data, it is suggested that $Fe_x(Ca)_yCO_3$ and akagenite $Fe_8O_8(OH)_8Cl_{1.35}$ are both present in this layer. The interface between the scale and the steel substrate in sample 1Cr is less rough compared to that in sample 0Cr.

Contrary to the corroded surface morphology for samples 0Cr and 1Cr, a broken corrosion scale in the form of isolated patches is observed on sample 3Cr (see Fig. 9e). The areas between the patches probably correspond to locations of prior austenite grain boundaries. Some cracks seem to propagate through the entire scale thickness, causing spallation of patches. A highly irregular and porous scale with variation in scale thickness is seen in the longitudinal section of sample 3Cr (Fig. 9f). Based on the EDS results (see supplementary Fig. S3), it is concluded that the scale is comprised of Ca, C, O and a small amount of Fe. A thin layer rich in Fe and O is observed close to the steel surface, which can potentially be akagenite or some other oxide/hydroxides of iron. The interface between the scale and the steel surface in sample 3Cr is much smoother and uniform compared to the other samples.

DISCUSSION

Designing Cr-containing steel requires consideration of how Cr content affects CO_2 corrosion behavior. In the following, the influence of the Cr content in low alloy steel on CO_2 corrosion and on the development of scales in simulated produced water at 80 °C is discussed based on the results obtained using several electrochemical methods and material characterization techniques.

The impact of Cr concentration on corrosion kinetics

According to the LPR and EIS results (Figs. 4a, 6c), adding 3%Cr is adequate to enable stronger corrosion resistance in the tested environment than the samples containing 0%Cr and 1%Cr in the chemical composition. This effect of the Cr content is only noticeable for the first 2 days of exposure, after which the corrosion behavior changes and sample 0Cr exhibits greater corrosion resistance. These changes are rationalized as follows.

The difference in the inherent corrosion resistance between samples 1Cr and 3Cr is more significant than that between samples 0Cr and 1Cr. The presence of the $Cr(OH)_3$ pre-passivation
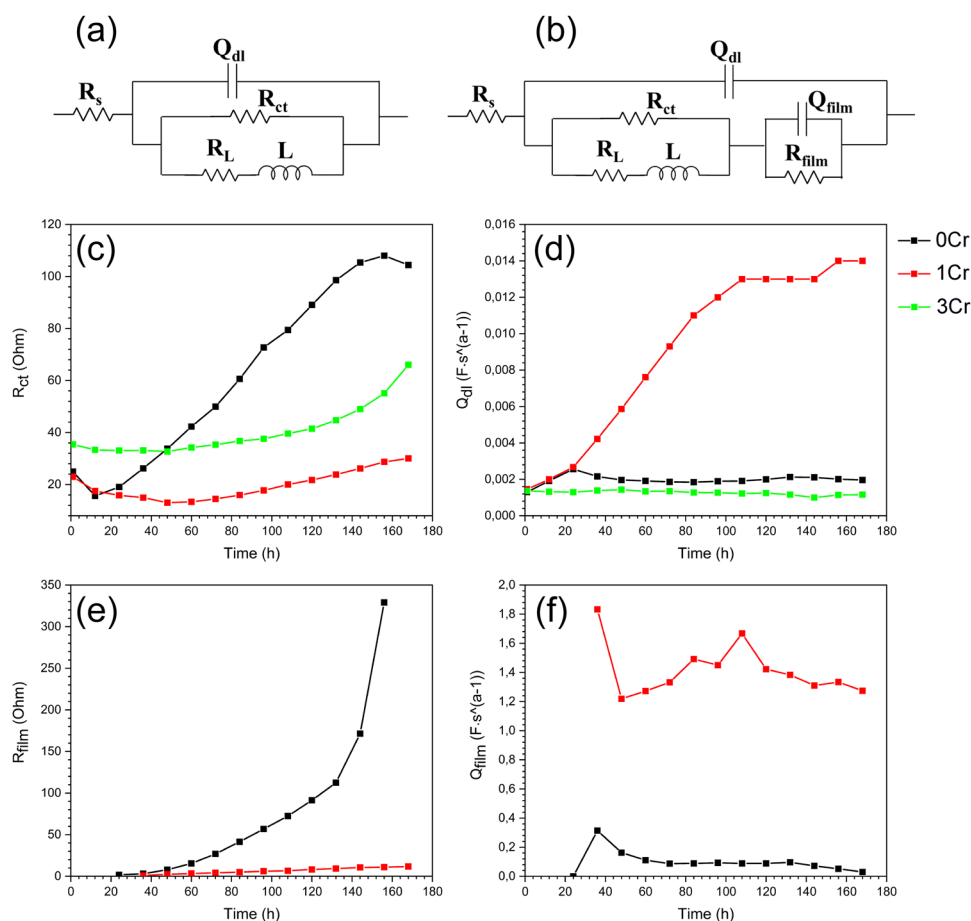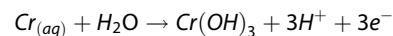
Fig. 6 Corrosion systems modelling using equivalent circuits and evaluating the changes in various surface features affecting corrosion behavior. Equivalent circuits used for fitting the EIS results for samples (**a**) without corrosion scale and (**b**) with corrosion scale, and individual components as a function of exposure time to the electrolyte: (**c**) R_{ct}; (**d**) Q_{dl}; (**e**) R_{film} and (**f**) Q_{film}. The Nyquist plot for sample 3Cr did not reveal the presence of a capacitive loop in the LF region and was fitted using equivalent circuit shown in (**a**). Therefore, film properties (R_{film} and Q_{film}) could not be determined for sample 3Cr.

layer on the surface of sample 3Cr, as observed through the XPS spectra (Fig. 3), can explain such significant variations in the corrosion rate between samples 1Cr and 3Cr. The pseudo-capacitive inductive loop shown in the LF region of the Nyquist plots for sample 3Cr also validates the pre-passivation (see Fig. 5c). The fact that only sample 3Cr exhibits this loop can be explained by the adsorption of marginally protective intermediate species on the surface of this sample. According to Xu et al.[19], 3%Cr is sufficient to produce a thin $Cr(OH)_3$ layer that causes pre-passivation, which is in agreement with our XPS results. In another study[34], anodic potentiodynamic tests also revealed the pre-passivation properties of the 3Cr steel. Hence, it can be assumed that each specific corrosion environment has a critical Cr content. Pre-passivation significantly enhances the corrosion resistance when the Cr content is higher than the critical Cr content.

During the initial dissolution stage, the small difference in corrosion resistance between samples 0Cr and 1Cr can be attributed to the leaching of Cr^{3+} ions along with Fe^{2+} ions in the solution. This results in a high amount of Cr^{3+} ions present in the close vicinity of the surface. Hydration of these Cr^{3+} ions results in the development of a thin semi-passive $Cr(OH)_3$ layer, which provides a small degree of inhibition as opposed to sample 0Cr in agreement with the results found in literature[40]. However, the poor corrosion resistance of sample 1Cr can be related to the smaller grain size in this sample, 0.6 μm, compared to the other samples, 1.3–1.5 μm (see Fig. 2d). High angle boundaries are crystalline defects characterized by a high energy. Therefore, it is

reasonable that a higher surface area of such boundaries per unit volume in sample 1Cr can result in more severe anodic dissolution[10,11,41–45]. Our findings are consistent with observations of Ko et al.[46], who also found that regions containing small grains are more prone to corrosion. Nevertheless, since the grain size is similar in samples 0Cr and 3Cr, the chemical composition is considered to be a more important factor influencing the variance in corrosion rates observed in the present work.

The most crucial step for improved corrosion resistance is creating a relatively passive $Cr(OH)_3$ layer early in the corrosion process. The amount of free Cr that is accessible for hydrolysis determines the tentative mechanism by which Cr inhibits CO_2 corrosion. $Cr(OH)_3$ will develop during the corrosion of low-Cr steel as a result of the hydrolysis of free Cr (Eq. (1))[47].

$$Cr_{(aq)} + H_2O \rightarrow Cr(OH)_3 + 3H^+ + 3e^-$$

Both the microstructure and the chemical composition of sample 3Cr contribute to the level of free Cr in the solid solution. The microstructure can impact pre-passivation and consequently the corrosion performance in addition to the Cr content. It is expected that small adjustments to the other element concentration can make $Cr(OH)_3$ formation more likely, thus improving inherent corrosion resistance. The lower carbon content and addition of carbide-forming substances such as Nb, Ti, etc. enable a larger concentration of Cr in solid solution for pre-passivation[30]. Therefore, compared to samples 0Cr and 1Cr, sample 3Cr initially
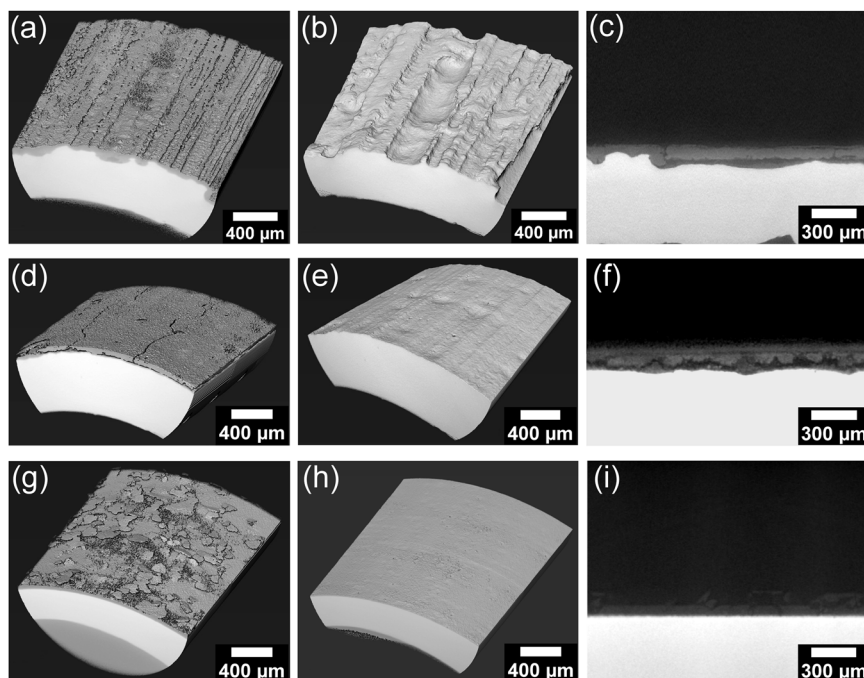
Fig. 7 Corroded surface morphology analyzed using X-ray microscopy. Results of the XRM analysis of the samples exposed to the electrolyte for 7 days: (**a**–**c**) sample 0Cr; (**d**–**f**) sample 1Cr and (**g**–**i**) sample 3Cr. Images (**b**, **e**, **h**) are 3D representations showing the steel surface without the corrosion scale; Images (**c**, **f**, **i**) present computer-generated 2D slices along the longitudinal axis of the samples with both the steel and scales shown.
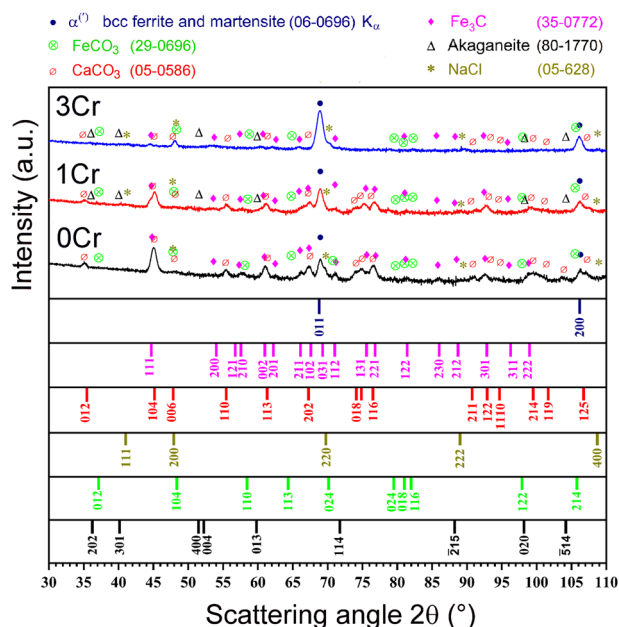

Fig. 8 X-ray diffractograms for the samples corroded in the electrolyte.

exhibits better inherent corrosion resistance, as is evident from Figs. 4a, 6c.

The effect of Cr content on scale formation

When different cations (including dissolved Fe^{2+}) are present in the electrolyte, they interact with the anions produced by cathodic reduction processes to form different types of corrosion products and scales. According to X-ray diffractograms in Fig. 8,

mixed $Fe(Ca)CO_3$ carbonates rich in Ca and/or Fe and akagenite $Fe_8O_8(OH)_8Cl_{1.35}$ are the principal corrosion products with residual cementite remaining from the initial microstructure. Additionally, the composition of the scale and the phase distribution vary depending on the Cr content. The onset of siderite precipitation is reliant on the Fe^{2+} supersaturation, as described in our previous work[10]. As follows from the R_p and R_{film} values in Figs. 4, 6e, the faster precipitation of protective siderite in sample 0Cr is due to the higher rate of Fe dissolution in this sample. High Fe^{2+} dissolution enables nearly complete substitution of pure $CaCO_3$ with mixed carbonate $Fe_xCa_yCO_3$ rich in Fe by allowing a high fraction of Fe^{2+} ions to replace Ca^{2+} ions from the $CaCO_3$ phase[48]. The precipitation of the protective siderite is also indicated by a rapid increase in R_{film} and a decline in Q_{film} (see Fig. 6f). However, under these conditions (the presence of Ca^{2+} ions in the electrolyte and low bulk pH), the $Fe_xCa_yCO_3$ crystals are more irregular cuboidal shaped and thus not able to show protectiveness[8,27].

For sample 1Cr, the protective siderite layer formation is slower than for sample 0Cr, allowing the deposition of $CaCO_3$ in large quantities and also allowing the formation of a higher amount of akagenite as observed in the XRD data (see Fig. 8). A small amount of Cr^{3+} ions is released in the solution along with the release of Fe^{2+} ions during the corrosion process (see Section 'The impact of Cr concentration on corrosion kinetics'). As suggested in the literature[49], the presence of Cr in the solution can act as a catalyst for the nucleation of siderite, but Cr can also lower the pH of the solution. Thus, the competition between these two different effects determines the scale formation. Under the tested condition, the rate of decrease in $FeCO_3$ precipitation prevails over the increase in the nucleation of $FeCO_3$ due to the presence of Cr^{3+} ions. Therefore, siderite precipitation is delayed in sample 1Cr compared to that in sample 0Cr. On the other hand, ref. [50] asserts that the reaction of Fe^{2+} ions in the electrolyte can result in the formation of semicrystalline FeO and FeOOH phases. As corrosion progresses, positive ions are created on the steel
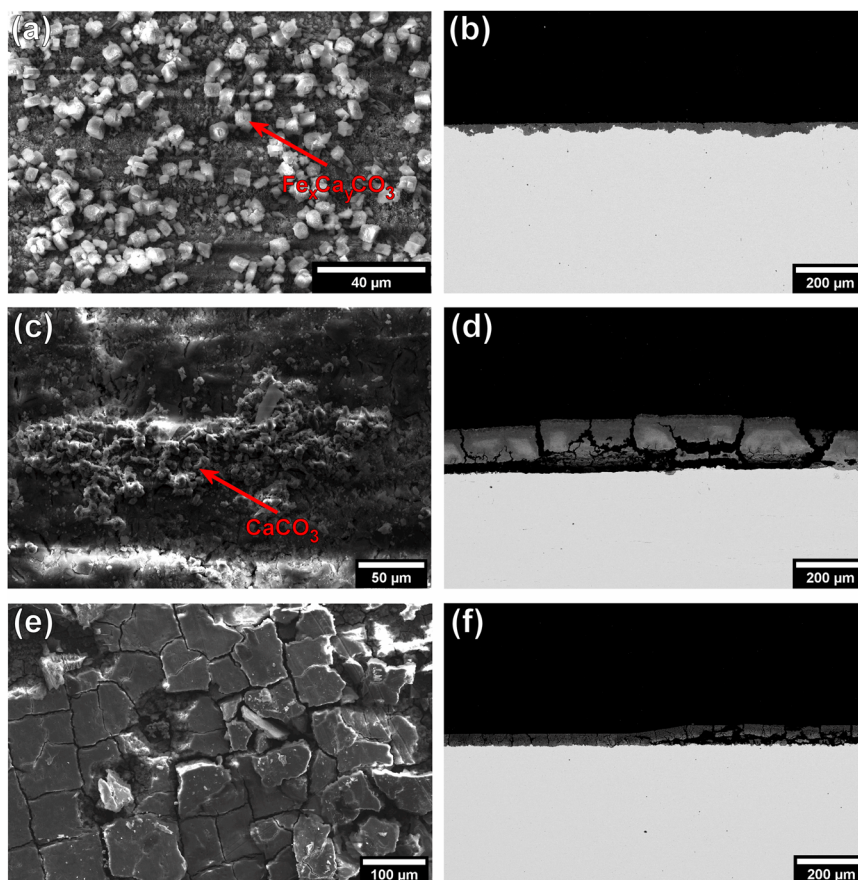
Fig. 9 Morphology of the corrosion products and scales developed on the corroded samples. SEM images showing corrosion products developed during 7-day exposure to the electrolyte: (**a**, **b**) sample 0Cr; (**c**, **d**) sample 1Cr and (**e**, **f**) sample 3Cr. Images in (**a**, **c**, **e**) show the corroded surface morphology. Images (**b**, **d**, **f**) are taken from the longitudinal section of the samples.

surface, while negative ions, such as Cl^-, penetrate through the surface, causing electrical imbalance[51]. The FeOOH phase forms when a specific Cl^- ion concentration is reached. Strong reducing agents such as FeOOH, which accelerate corrosion, also encourage the formation of akaganeite when paired with high Cl^- ion concentrations[50]. As seen in Fig. 6e, f, these products develop and precipitate at various exposure times, causing the scale to be layered with varying thickness (Fig. 7f) similar to the corrosion film observed for the QT sample in our previous work[52]. The layers are not connected since these corrosion products do not expand much, resulting in scale with high porosity and weak adherence to the steel surface, as seen in the SEM images taken from the longitudinal section (Fig. 9d). Moreover, the initial constant R_{film} value (see Fig. 6e) and the gradual increase in Q_{film} (see Fig. 6f) can be attributed to the competition between scale development and disintegration associated with the scaling process. Therefore, despite being thicker than in sample 0Cr (see Fig. 9b, d), the scale in sample 1Cr has weak resistance to corrosion (see Fig. 6e). Thus, although siderite is present in the scale of sample 1Cr (see Fig. 8), this sample demonstrates reduced corrosion resistance during long-term exposures.

In contrast to samples 0Cr and 1Cr, sample 3Cr has very good inherent corrosion resistance. In the latter sample, the siderite precipitation is delayed by poor Fe dissolution and high Cr^{3+} ion levels near the steel surface, hence the protective scale development is incomplete for sample 3Cr even after 7-day exposure (see Figs. 5c, 8). Based on the small peak intensity in the X-ray diffractogram, it is concluded that only a small amount of mixed $Fe_xCa_yCO_3$ is present in the scale formed on the surface of this sample. Compared to the other samples, the overall scale in

sample 3Cr is thin, porous and contains cracks (see Fig. 7e and Fig. 9e, f). The presence of an inductive loop at LF for the 3Cr sample (see Fig. 5c) indicates that the small amount of scale formed is not able to completely cover the whole sample surface, i.e. the scale is not fully protective. In contrast, a thick and compact protective corrosion film forms on the surface of sample 0Cr after 7 days of exposure, significantly increasing the corrosion resistance of this sample compared to that of sample 3Cr (as evaluated from the LPR results in Fig. 4b and the EIS measurements in Fig. 5a). However, the scale on sample 3Cr reveals a significant amount (7 wt%) of Cr detected by EDS after 7 days of exposure (see supplementary Fig. S3). Once the scale has formed, the presence of Cr in the scales of sample 3Cr makes the scales much more protective than the scales in the other samples. Correspondingly, after 28 days of exposure, the corrosion resistance of sample 3Cr is approximately twice as strong as the resistance of sample 0Cr (see the LPR curve in Fig. 4b).

The efffect of Cr content on the corrosion mode

Fe dissolution is not significant in sample 3Cr because of pre-passivation resulting in a low corrosion rate, so that the corroded surface appears smooth and uniform (see Figs. 7h, 9f). On the other hand, samples 0Cr and 1Cr both exhibit high corrosion rates, and the dissolution of Fe through selective corrosion creates rather rough surfaces in these samples (see Fig. 7b, e). This is further demonstrated by the rapid rise in Q_{dl} with time (Fig. 6d) for samples 0Cr and 1Cr, while Q_{dl} for sample 3Cr is nearly constant. Because of increasing surface roughness, the anodic surface area increases, which leads to an increase in Q_{dl}.
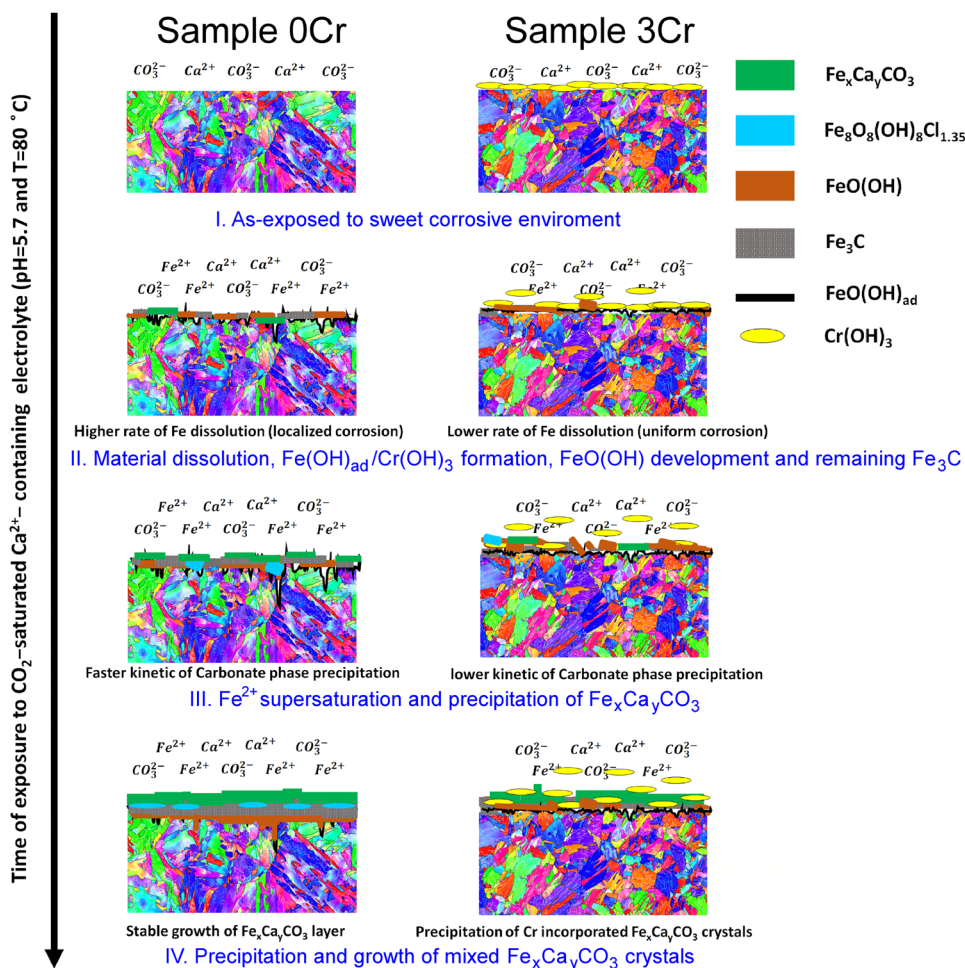
Fig. 10 Schematic representation of the proposed CO_2 corrosion mechanism of low alloy steel with significantly different concentrations of Cr (samples 0Cr and 3Cr) and corresponding scale initiation and development. The investigated tempered-martensite steels surfaces are illustrated using fragments of orientation maps shown in Fig. 2b, f.

The XRM images for samples 0Cr and 1Cr show several craters, which are thought to be caused by a mesa corrosion attack. The extent of mesa corrosion is found to decrease as the Cr content in the steel increases. The presence of Cr and $Cr(OH)_3$ in the scale is thought to be the cause of this phenomenon. The carbonate film seems to be less vulnerable to the localized attack when Cr is present. Although localized attacks can start in every Cr-containing low alloy steel sample, protective corrosion films are able to regenerate faster in sample 3Cr than in the other samples. As a result, localized attack and selective corrosion are decreased by increasing Cr content. Our findings are consistent with the results of Nyborg and Dugstad, who showed that due to the ability to rebuild protective films, the localized attack in low alloy steels with increased Cr content is less harmful than in steels with low concentrations of Cr[53].

To summarize the discussion in this and two previous subsections, Fig. 10 shows schematically the proposed CO_2 corrosion behavior and corresponding scale development mechanisms in Cr-free and Cr-rich low alloy steels. This figure illustrates that the addition of Cr influences both the corrosion behavior and the corrosion mode. Although the conducted static CO_2 corrosion tests reveal high corrosion resistance for sample 3Cr, the poor adherence to scale can hamper its corrosion resistance in dynamic conditions. Also, even though sample 0Cr and sample 1Cr show better scale adhesion under static conditions, the enhanced shear stress due to dynamic conditions might cause spalling of the formed protective scale. This should be taken into account when determining the balance between cost and corrosion resistance of low alloy steels utilized in products for the oil and gas industry and for other applications in corrosive environments.

METHODS

Materials

The chemical composition of the API L80 steel samples with different Cr content, 0, 1, and 3 wt% Cr (samples 0Cr, 1Cr, and 3Cr, respectively), used in this work is shown in Table 1. The samples were received after oil-quenching and tempering. Hollow cylindrical ⌀5 mm specimens with a height of 15 mm were cut from the as-received material. In order to facilitate X-ray transmission for X-ray microscopy, the wall thickness of the specimen was limited to 0.5 mm. This was done by machining a ⌀4 mm thread extended down to 3 mm from the top of the specimens.

Electrochemical measurements

Electrochemical tests were carried out in a glass cell with an electrolyte volume of 1.5 L using a standard three-electrode set-up with Ag/AgCl as a reference electrode and platinum wire as a counter electrode. The electrolyte used for the investigation was simulated produced water (SPW) saturated with CO_2 (specified in Table 2). Prior to specimen immersion, the electrolyte was

Table 1. Chemical composition (wt%) of the tested samples.

Sample	C	Cr	Mn	Mo	P	Si	S	Ni	Cu	Fe
0Cr	0.43	–	1.9	–	0.03	0.45	0.03	0.25	0.35	base
1Cr	0.40	1.1	0.8	0.2	0.03	0.20	0.03	0.25	0.35	base
3Cr	0.11	3.2	0.7	0.6	0.02	0.40	0.005	0.15	–	base

Table 2. Ionic composition of the electrolyte.

Unit	Na^+	Cl^-	Ca^{2+}	HCO_3^-	Fe^{2+}
Molarity	1.13	1.43	0.15	0.015	0.0016
ppm	27450	53000	6012	917	90

deaerated by nitrogen gas purging for 12 h. The gas was then switched to CO_2 and continued purging for 4 h to reach initial saturation, after which the sample was immersed. The purging of CO_2 was then continued throughout the entire duration of the experiment, so that the solution was always saturated with CO_2. Thus, the total amount of CO_2 in the water phase was constant at ~25 mmol/kg (as calculated by the pHSim software).

The initial pH of the solution was approximately 5.7, and the experiments were conducted under the CO_2 saturation condition at 80 °C.

The surface used for corrosion experiments was polished using a 1 μm diamond suspension and then cleaned with ethanol before corrosion measurements. The dried specimens were mounted on a specimen holder and immersed in the test solution. Both the flat surface and the outside curved surface with a total area of 2.55 cm^2 were exposed to the electrolyte. The initial test duration for each sample was 7 days, and two additional tests were conducted for samples 0Cr and 3Cr with a total duration of 28 days. For the electrochemical experiments, one-hour open circuit potential (OCP) stabilization was used. EIS and linear polarization resistance measurements were then carried out in one cycle after every hour. The EIS measurements were performed by applying an AC signal with ± 10 mV vs OCP amplitude in a frequency range between 10 kHz and 10 mHz. Simultaneously, the corrosion potential E_{corr} and the corrosion resistance were monitored using LPR measurements at 1 h intervals. For the LPR measurements, a potential range of ± 10 mV over OCP at a scan rate of 0.167 mV/s was used as defined by the ASTM-G59 standard. All the tests were repeated three times to enable statistical analysis.

X-ray diffraction

The phase composition of the initial samples and corrosion products induced by CO_2 electrochemical exposure was analyzed using a Bruker D8 Advance lab source X-ray diffractometer. The instrument was operated at 35 kV and 50 mA using Cr-Kα radiation (λ = 0.22909 nm) in the parallel beam geometry configuration. The X-ray diffractograms were acquired in the angular scattering range (2θ = 30–110°). The Δ2θ step size and the acquisition time per step were 0.03° and 12 s, respectively.

Electron microscopy, EBSD and EDS

Prior to the initial microstructural analysis, the samples were etched in 2% nital solution followed by rinsing in deaerated water and ethanol and dried. Backscattered electron images of the as-received samples were acquired using a Quanta FEG 250 Analytical ESEM at an accelerating voltage of 20 kV. The etched surface was mechanically ground and electrochemically polished in Struers A2 solution, and EBSD data were obtained using a Zeiss Sigma 300 scanning electron microscope equipped with a C-Nano detector from Oxford Instruments. The step size for the EBSD measurements was 50 nm.

The CO_2-corroded samples were characterized both on the top surface and in the sample longitudinal section. To enable SEM examination of the longitudinal section, the specimens were embedded using cold mounting resin to avoid damage on the corroded surface and then sliced, followed by grinding (using ethanol ≥ 99.9% as a lubricant) and final mechanical polishing in a Struers Tegramin-25 machine using the 1 μm diamond suspension. The samples were carbon coated to prevent charging of non-conductive corrosion products during SEM investigations. After acquiring SEM micrographs, the corrosion products were analyzed using EDS using an X-Max detector from Oxford Instruments.

X-ray photoelectron spectroscopy

XPS spectra of the non-corroded samples were determined using a K-Alpha XPS-Thermo Scientific system. The spectra were collected using an Al Kα X-ray source (1486.6 eV) radiation with an overall energy resolution of ~0.8 eV. Survey spectra were recorded in the 200 eV kinetic energy range with 1 eV steps, after which high-resolution scans (C 1 s, O 1 s, Cr 2p and Fe 2p) were conducted with 0.1 eV steps. The high resolution scans were calibrated using the reference C 1 s and Fe 2p signals. Ion beam etching was performed using a voltage of 200 eV and high current which accounts for 0.02 nm/s etching of reference Ta_2O_5. High resolution XPS depth profile analysis was conducted at several depths where the number N of each level corresponds to N×5 s of etching.

X-ray microscopy

A Zeiss Xradia 410 Versa system operated at 150 kV and 10 W was used for X-ray microscopy, where a high-energy filter HE3 was applied to filter out low-energy photons in order to enhance the reconstructed image quality. High spatial resolution XRM images were acquired from three different surface areas of the CO_2-corroded samples using a 4 × objective lens. The XRM images were recorded from 3201 projections, where the exposure time per projection was 22 s. A pixel size of 2.1 μm was obtained after 2 × 2 binning. A filtered back-projection algorithm developed by Feldkamp et al.[54] was applied for the analytical image reconstruction using an in-built software package from Zeiss. The Avizo software from ThermoFisher Scientific was used for processing, 3D visualization and analysis of the obtained data sets.

DATA AVAILABILITY

The data that support the findings of this study are available on request from the corresponding author (kkgup@dtu.dk) upon reasonable request.

REFERENCES

1. Kane, R. D. Corrosion in Petroleum Production Operations. in *ASM Handbook, Volume 13C: Corrosion: Environments and Industries* vol. **13** 922–966 (ASM International, 2006).
2. Popoola, L., Grema, A., Latinwo, G., Gutti, B. & Balogun, A. Corrosion problems during oil and gas production and its mitigation. *Int. J. Ind. Chem.* **4**, 35 (2013).
3. Wu, Q., Zhang, Z., Dong, X. & Yang, J. Corrosion behavior of low-alloy steel containing 1% chromium in CO_2 environments. *Corros. Sci.* **75**, 400–408 (2013).
4. Pfennig, A. & Kranzmann, A. Reliability of pipe steels with different amounts of C and Cr during onshore carbon dioxide injection. *Int. J. Greenh. Gas. Control* **5**, 757–769 (2011).

5. Nesic, S., Postlethwaite, J. & Olsen, S. An Electrochemical model for prediction of corrosion of mild steel in aqueous carbon dioxide solutions. *Corrosion* **52**, 280–294 (1996).

6. Nešić, S. Key issues related to modelling of internal corrosion of oil and gas pipelines - A review. *Corros. Sci.* **49**, 4308–4338 (2007).

7. Li, W., Xiong, Y., Brown, B., Kee, K. E. & Nesic, S. Measurement of wall shear stress in multiphase flow and its effect on protective FeCO₃ corrosion product layer removal. *Nace Corrosion*, Paper No. NACE-2015-5922, 1–15 (2015).

8. Tanupabrungsun, T., Brown, B., Nesic, S. & Technology, M. Effect of pH on CO₂ corrosion of mild steel at elevated temperatures. *Nace corrosion, Paper No. NACE-2013-2348,* 1–11 (2013).

9. López, D. A., Pérez, T. & Simison, S. N. The influence of microstructure and chemical composition of carbon and low alloy steels in CO₂ corrosion. A state-of-the-art appraisal. *Mater. Des.* **24**, 561–575 (2003).

10. Gupta, K. K., Haratian, S., Gupta, S., Mishin, O. V. & Ambat, R. The effect of cooling rate-induced microstructural changes on CO₂ corrosion of low alloy steel. *Corros. Sci.* **209**, 110769 (2022).

11. Gupta, K. K., Yazdi, R., Styrk-Geisler, M., Mishin, O. V. & Ambat, R. Effect of microstructure of low-alloy steel on corrosion propagation in a simulated CO₂ environment. *J. Electrochem. Soc.* **169**, 1–13 (2022).

12. Edmonds, D. V. & Cochrane, R. C. The effect of alloying on the resistance of carbon steel for oilfield applications to CO₂ corrosion. *Mater. Res.* **8**, 377–385 (2005).

13. Li, W., Xu, L., Qiao, L. & Li, J. Effect of free Cr content on corrosion behavior of 3Cr steels in a CO₂ environment. *Appl. Surf. Sci.* **425**, 32–45 (2017).

14. Park, J. H., Seo, H. S., Kim, K. Y. & Kim, S. J. The effect of Cr on the electrochemical corrosion of high Mn steel in a sweet environment. *J. Electrochem. Soc.* **163**, C791–C797 (2016).

15. Chen, T., Xu, L., Chang, W., Zhang, L. & Beijing, T. Study on factors affecting low Cr alloy steels in a CO₂ corrosion system. *Nace Corrosion.* Paper No. NACE-11074, 1–14 (2011).

16. Guo, S., Xu, L., Zhang, L., Chang, W. & Lu, M. Corrosion of alloy steels containing 2% chromium in CO₂ environments. *Corros. Sci.* **63**, 246–258 (2012).

17. Hassani, S. et al. Wellbore integrinanoty and corrosion of low alloy and stainless steels in high pressure CO₂ geologic storage environments: An experimental study. *Int. J. Greenh. Gas. Control* **23**, 30–43 (2014).

18. Takabe, H. & Ueda, M. The formation behavior of corrosion protective films of low Cr bearing steels in CO₂ environments. *Nace Corrosion, Paper No. NACE-01066, 1–15* (2001).

19. Xu, L., Wang, B., Zhu, J., Li, W. & Zheng, Z. Effect of Cr content on the corrosion performance of low-Cr alloy steel in a CO₂ environment. *Appl. Surf. Sci.* **379**, 39–46 (2016).

20. Kermani, M. B., Gonzales, J. C., Linne, C., Dougan, M. & Cochrane, R. Development of low carbon Cr-Mo steels with exceptional corrosion resistance for oilfield applications. *Nace Corrosion, Paper No. NACE-01065, 1–22* (2001).

21. Ueda, M. & Ikeda, A. Effect of microstructure and Cr content in steel on CO₂ corrosion. *Nace Corrosion, Paper No. NACE-96013, 1–16* (1996).

22. Li, C., Xiang, Y., Song, C. & Ji, Z. Assessing the corrosion product scale formation characteristics of X80 steel in supercritical CO₂-H₂O binary systems with flue gas and NaCl impurities relevant to CCUS technology. *J. Supercrit. Fluids* **146**, 107–119 (2019).

23. Kermani, M. B. et al. Development of superior corrosion resistance 3%Cr steels for downhole applications. *Nace Corrosion, Paper No. NACE-03116, 1-14* (2003).

24. Kermani, M. B., Gonzles, J. C., Turconi, G. L. & Perez, T. In-field corrosion performance of 3%Cr steels in sweet and sour downhole production and water injection. *Nace Corrosion,* Paper No. NACE-04111, 1-19 (2004).

25. Cabrini, M., Hoxha, G., Kopliku, A. & Lazzari, L. Prediction of CO₂ corrosion in Oil and Gas wells. Analysis of some case histories. *Nace Corrosion, Paper no. NACE-98024,* 1-13 (1998).

26. Nyborg, R., Dugstad, A. & Droenen, P. Effect of chromium on mesa corrosion of carbon steel. *Book-institute materials* **715**, 63–69 (1998).

27. Dugstad, A. Mechanism of protective film formation during CO₂ corrosion of carbon steel. *Nace Corrosion, Paper No. NACE-98031, 1-11* (1998).

28. Dugstad, A., Hemmer, H. & Seiersten, M. Effect of steel microstructure upon corrosion rate and protective iron carbonate film formation. *Corrosion* **57**, 369–378 (2000).

29. Denpo, K. & Ogawa, H. Effects of nickel and chromium on corrosion rate of linepipe steel. *Corros. Sci.* **35**, 285–288 (1993).

30. Kermani, M. B. & Morshed, A. Carbon Dioxide Corrosion in Oil and Gas Production —A Compendium. *Corrosion* **59**, 659–683 (2003).

31. Carvalho, D. S., Joia, C. J. B. & Mattos, O. R. Corrosion rate of iron and iron-chromium alloys in CO₂ medium. *Corros. Sci.* **47**, 2974–2986 (2005).

32. Bai, Z. Q., Chen, C. F., Lu, M. X. & Li, J. B. Analysis of EIS characteristics of CO₂ corrosion of well tube steels with corrosion scales. *Appl. Surf. Sci.* **252**, 7578–7584 (2006).

33. Xu, L. N. et al. Influence of microstructure on mechanical properties and corrosion behavior of 3%Cr steel in CO₂ environment. *Mater. Corros.* **63**, 997–1003 (2012).

34. Zhu, J. et al. Essential criterion for evaluating the corrosion resistance of 3Cr steel in CO₂ environments: Prepassivation. *Corros. Sci.* **93**, 336–340 (2015).

35. Muraki, T., Hara, T., Nose, K. & Asahi, H. Effects of chromium content up to 5% and dissolved oxygen on CO₂ corrosion. *Nace Corrosion, Paper No. NACE-02272, 1-13* (2002).

36. Ma, L. et al. Passivation mechanisms and pre-oxidation effects on model surfaces of FeCrNi austenitic stainless steel. *Corros. Sci.* **167**, 1–12 (2020).

37. Larsson, A. et al. Thickness and composition of native oxides and near-surface regions of Ni superalloys. *J. Alloy. Compd.* **895**, 162657 (2022).

38. Gardin, E., Zanna, S., Seyeux, A., Allion-Maurer, A. & Marcus, P. XPS and ToF-SIMS characterization of the surface oxides on lean duplex stainless steel – Global and local approaches. *Corros. Sci.* **155**, 121–133 (2019).

39. Desimoni, E., Malitesta, C., Zambonin, P. G. & Rivière, J. C. An x-ray photoelectron spectroscopic study of some chromium-oxygen systems. *Surf. Interface Anal.* **13**, 173–179 (1988).

40. Hua, Y., Mohammed, S., Barker, R. & Neville, A. Comparisons of corrosion behaviour for X65 and low Cr steels in high pressure CO₂-saturated brine. *J. Mater. Sci. Technol.* **41**, 21–32 (2020).

41. Rafiee, E., Farzam, M., Golozar, M. A. & Ashrafi, A. An investigation on dislocation density in cold-rolled copper using electrochemical impedance spectroscopy. *ISRN Corrosion,* Article ID 921825, 1-6 (2013).

42. Li, W. & Li, D. Y. Variations of work function and corrosion behaviors of deformed copper surfaces. *Appl. Surf. Sci.* **240**, 388–395 (2005).

43. Dwivedi, D., Lepková, K. & Becker, T. Carbon steel corrosion: a review of key surface properties and characterization methods. *RSC Adv.* **7**, 4580–4610 (2017).

44. Hanza, S. S., Štic, L., Liverić, L. & Špada, V. Corrosion behaviour of tempered 42CrMo4 Steel. *Mater. Tehnol.* **55**, 427–433 (2021).

45. Escrivà-Cerdán, C. et al. Effect of tempering heat treatment on the CO₂ corrosion resistance of quench-hardened Cr-Mo low-alloy steels for oil and gas applications. *Corros. Sci.* **154**, 36–48 (2019).

46. Ko, M., Ingham, B., Laycock, N. & Williams, D. E. In situ synchrotron X-ray diffraction study of the effect of microstructure and boundary layer conditions on CO₂ corrosion of pipeline steels. *Corros. Sci.* **90**, 192–201 (2015).

47. Chen, C. F., Lu, M. X., Sun, D. B., Zhang, Z. H. & Chang, W. Effect of chromium on the pitting resistance of oil tube steel in a carbon dioxide corrosion system. *Corrosion* **61**, 594–601 (2005).

48. Rizzo, R. & Ambat, R. Effect of initial CaCO₃ saturation levels on the CO₂ corrosion of 1Cr carbon steel. *Mater. Corros.* **72**, 1076–1090 (2021).

49. Ko, M., Ingham, B., Laycock, N. & Williams, D. E. In situ synchrotron X-ray diffraction study of the effect of chromium additions to the steel and solution on CO₂ corrosion of pipeline steels. *Corros. Sci.* **80**, 237–246 (2014).

50. Yang, Y. et al. Characterization, formation and development of scales on L80 steel tube resulting from seawater injection treatment. *J. Pet. Sci. Eng.* **193**, 107433 (2020).

51. Tomio, A. et al. Role of alloyed copper on corrosion resistance of austenitic stainless steel in H₂S-Cl⁻ environment. *Corros. Sci.* **81**, 144–151 (2014).

52. Haratian, S. et al. Ex-situ synchrotron X-ray diffraction study of CO₂ corrosion-induced surface scales developed in low-alloy steel with different initial microstructure. *Corros. Sci.* **222**, 1–13 (2023).

53. Nyborg, R. & Dugstad, A. Mesa corrosion attack in carbon steel and 0.5% chromium steels. *Nace Corrosion*, Paper No. NACE-98029, 1-10 (1998).

54. Feldkamp, L. A., Davis, L. C. & Kress, J. W. Practical cone-beam algorithm. *Opt. Soc. Am.* **1**, 612–619 (1984).

ACKNOWLEDGEMENTS

AUTHOR CONTRIBUTIONS

K.K.G.: Methodology, Investigation, Formal analysis, Writing – original draft. S.H.: Investigation, Formal analysis, Writing – original draft. O.V.M.: Investigation, Formal analysis, Writing – review & editing. R.A.: Conceptualization, Resources, Writing – review & editing, Supervision

COMPETING INTERESTS

The authors declare no competing interests.

ADDITIONAL INFORMATION

Supplementary information The online version contains supplementary material available at https://doi.org/10.1038/s41529-023-00393-y.

Correspondence and requests for materials should be addressed to Kapil K. Gupta.

Reprints and permission information is available at http://www.nature.com/reprints

Publisher's note Springer Nature remains neutral with regard to jurisdictional claims in published maps and institutional affiliations.